J Mater Sci (2006) 41:4445–4453
DOI 10.1007/s10853-006-0089-5

Electron microscope weak-beam imaging of stacking fault tetrahedra: observations and simulations

M. L. Jenkins · Z. Zhou · S. L. Dudarev · A. P. Sutton · M. A. Kirk

Received: 28 November 2005 / Accepted: 13 February 2006 / Published online: 29 June 2006
© Springer Science+Business Media, LLC 2006

Abstract Weak-beam diffraction-contrast electron microscope images of stacking-fault tetrahedra (SFT) have been simulated by solving numerically the Howie–Basinski equations, which are well suited for studying the dependence of image contrast on experimental parameters. These simulated images are in good qualitative agreement with experimental transmission electron micrographs. The visibility of small SFT and the relationship between measured image sizes and real SFT sizes are discussed.

Introduction

Nanometer-sized dislocation loops and other small point-defect clusters such as stacking-fault tetrahedra (SFT) are commonly found in quenched, deformed or irradiated materials. Such defects are often investigated by diffraction contrast methods in the transmission electron microscope (TEM). However severe difficulties in image interpretation arise for very small defects or complex dislocation configurations. Computer simulation of images is often used to aid image interpretation, but unfortunately existing computer codes are not fully suited to the simulation of images of complex defects under the experimental conditions often used in practice. In particular small clusters are often imaged using the weak-beam method because it offers improved contrast and resolution compared with other imaging conditions. We have developed an image simulation program based on the Howie–Basinski equations of dynamical diffraction theory in which the non-parallel propagation of diffracted electron beams is taken into account [1]. This approach is suited to the simulation of weak-beam images of small cluster since it does not make use of the column approximation, which is made in the Howie–Whelan equations and equivalent formulations of dynamical diffraction theory, and which may be poor for such conditions.

A possible alternative method of simulating diffraction contrast images of defects is to use the multi-slice approach, which is more commonly used to simulate high-resolution images. The multislice approach also avoids the column approximation. However, this approach is not convenient for simulating the contrast of defects with long-range elastic fields because it is essentially atomistic—the scattering from each atom is summed. The method is able to deal easily with strong local distortions, including stacking faults. However, in treating defects such as SFT and dislocation loops, which have long-range elastic strain fields due to dislocations it is necessary to specify atomic positions within a large supercell. Even in simple cases (for example, very small SFT, see below) this leads to very large computations, and so it is not possible to carry out systematic investigations of trends with the diffraction conditions, foil thickness and other imaging and defect

M. L. Jenkins (✉) · Z. Zhou
Department of Materials, University of Oxford, Parks Rd., Oxford OX1 3PH, UK
e-mail: mike.jenkins@materials.ox.ac.uk

S. L. Dudarev
EURATOM/UKAEA Fusion Association, Culham Science Centre, Oxfordshire OX14 3DB, UK

A. P. Sutton
Department of Physics, Imperial College, Prince Consort Rd., London SW7 2BZ, UK

M. A. Kirk
Materials Science Division, Argonne National Laboratory, Argonne, IL 60439, USA

parameters. For larger defects the supercell becomes unfeasibly large. In the Howie–Basinski approach the long-range elastic strain field is usually treated in a continuum model. This is much faster computationally, enabling systematic studies to be carried out relatively easily.

The basis of our program and some initial applications have been described in previous papers [2–4]. We used the program to carry out systematic studies of the weak-beam contrast of small dislocation loops in copper. Simulations were carried out for faulted Frank and perfect dislocation loops of size 2–10 nm with systematic variations in imaging parameters (the loop orientation, the diffraction vector, the deviation parameter, the loop depth and the foil thickness). Comparisons were made with experiments in ion-irradiated copper [5].

In the present paper we extend the simulations to SFT in copper and silver and compare the simulations with experimental weak-beam images of SFT.[1] Previous simulations of the contrast of SFT under dynamical imaging conditions have been reported by Saldin, Stathopoulos and Whelan [6] using the Howie–Whelan equations in the 2-beam approximation, but these authors did not attempt to simulate weak-beam images. Satoh et al. [7] have reported simulations of overlapping stacking-faults and stair-rod dislocations (but not complete SFT) using standard multi-beam diffraction theory, and simulations of the weak-beam image contrast of very small (~1 nm) SFT at the [110] orientation using the multi-slice method. Weak-beam images of SFT obtained by the multi-slice method have also been reported by Schäublin and co-workers [8, 9] for very limited cases.

The aims of our work were: (1) to compare simulated images with experimental images; (2) to find the sensitivity of the images to the various imaging parameters and to determine the optimum imaging conditions; (3) to compare the image size and the true size of the SFT for different sizes of SFT: and (4) to determine whether very small SFT (~2 nm) can be distinguished from small dislocation loops in experiments such as those of Jenkins et al. [5] alluded to above.

Simulation method

The distortion fields of SFT were calculated from linear elasticity theory using expressions for the strain fields of angular dislocation segments given by Joffe [10] and the method described previously by Saldin and Whelan [11]. In this method, which is shown schematically in Fig. 1, the SFT is constructed from four equilateral triangular edge loops lying on the four {111} faces of the SFT with Burgers vectors $^1/_{12}$ <111> and edges lying along <110> directions. Each triangular loop is constructed from three angular dislocation segments. Addition of the Burgers vectors of the loops at their lines of contact results in six stair-rod dislocations with Burgers vectors of type 1/6 < 110 >. The resulting distortion field was used to simulate electron microscope images in much the same way as for Frank loops as described in refs [2–4]. In the present simulations we use isotropic elasticity theory and elastic constants appropriate for copper or silver. The contribution to the beam amplitudes of the intrinsic stacking faults on the faces of the SFT was taken into account by introducing a phase shift of exp ($2\pi i$ **g.** $\mathbf{R}_{sf}$.) when a beam passed through a fault with displacement vector $\mathbf{R}_{sf}$ [12]. Anomalous absorption was included in the usual way by introducing an imaginary term to the Fourier components of potential (see [4] for details). All simulations shown below are weak-beam dark-field images for a microscope operating voltage of 100 kV, and include eight beams (0–7**g**).

In the following we have considered two diffraction geometries: (1) foil normal **n** = [111], and diffraction vector **g** = $2\bar{2}0$; and (2) **n** = [110] and **g** = 002. These orientations have been found by us to be suitable for imaging small SFT under weak-beam diffraction conditions. The same experimental conditions have been used by several previous investigators and so relevant weak-beam images of SFT are also available in the literature. In practice experimental micrographs are recorded a few degrees away from the exact pole orientation in order to avoid exciting non-systematic reflections when setting up

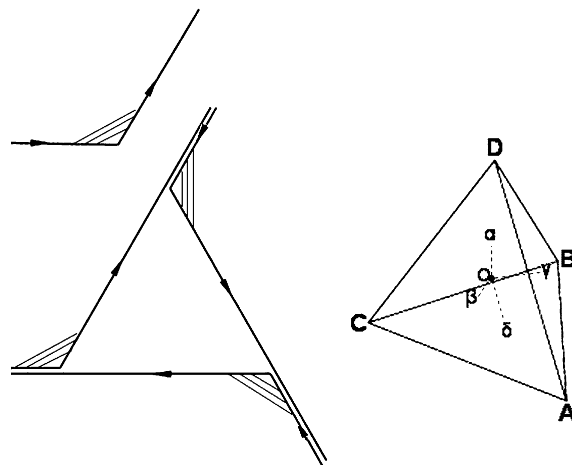

Fig. 1 Construction of an SFT from angular dislocation segments

[1] Some experimental images are for Au. In practice images are dominated by stacking-fault contrast which will not vary much from material to material, and so it was not thought worthwhile to repeat the simulations for Au which, being in the same column in the periodic table, is similar in many respects to Cu and Ag.

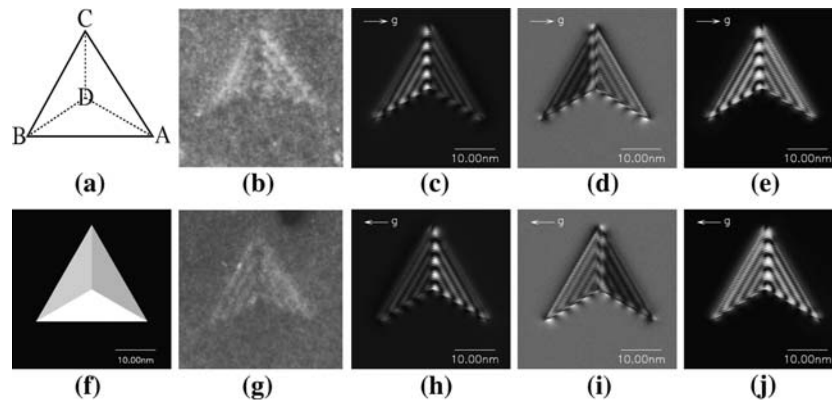

Fig. 2 SFT imaged with $\mathbf{g} = \pm\ 2\bar{2}0$ at $\mathbf{n} = [111]$. The image simulations (**c**)–(**e**) and (**h**)–(**j**) show images in $\mathbf{g} =\ 2\bar{2}0$ and $\mathbf{g} = \bar{2}20$ respectively for a large (28 nm) SFT in copper imaged under weak-beam conditions (**g**, 2.75 **g**) for three values of the foil thickness, 54.6 nm, 57 nm and 60 nm. Defect depth 30 nm. The orientation of the Thompson tetrahedron is shown in (**a**) and (**f**). Figures (**b**) and (**g**) show experimental images of an SFT in ion-irradiated silver

weak-beam diffraction conditions. This was not taken into account in the present simulations. However, in simulations of the weak-beam contrast of small Frank loops the effect on images of a small tilt away from the pole orientation was found to be small [4].

Results

Foil normal $\mathbf{n} = [111]$, and diffraction vector $\mathbf{g} = \pm\ 2\bar{2}0$

Simulations of weak-beam electron microscope images of SFT taken under these conditions are shown in Figs. 2 and 3. The three columns to the right of Fig. 2(c and h, d and i, and e and k) show simulated weak-beam images in $\mathbf{g} = \pm\ 2\bar{2}0$ of SFT of edge-length 28 nm located with their centroid at a depth of 30 nm in a foil ranging in depth from 54.6 to 60 nm and so encompassing one thickness-fringe oscillation. Figure 3 shows the dependence of the contrast on the defect depth for a 3 nm SFT in a foil of thickness 57 nm. It can be seen from Fig. 2 that larger SFT are imaged primarily by the non-overlapping stacking-faults on the two inclined {111} faces with $\mathbf{g.R}_{sf}$ non-integer, which are visible as fringes of depth periodicity ξ_g^{eff}. Here the effective extinction distance $\xi_g^{\mathrm{eff}} = \xi_g\ /(1 + w^2)$ where $w = |s_g\xi_g|$ is a dimensionless deviation parameter and ξ_g is the extinction distance. For weak-beam conditions with $w >> 5$, $\xi_g^{\mathrm{eff}} \approx |s|_g^{-1} \approx 5$ nm for $s_g = 2 \times 10^{-1}$ nm^{-1}. The contrast of smaller SFT also seems to come mostly but not entirely from the stacking-faults. The shape and sizes of the images are relatively stable, and this was confirmed by more extensive simulations not shown here. However the visibility even of large SFT may be quite low at foil thicknesses corresponding to a thickness fringe maximum, e.g. Fig 2d, i.[2] The stacking fault fringes may be weak, especially at defect depths near the foil centre.

Experimental images taken under similar conditions to the simulations of Figs. 2 and 3 have been shown by Jenkins [13] and many others, and examples are shown in Figs. 2b, g, 4 and 5. The experimental images are in good general agreement with the simulations. Figure 4 shows experimental images of large SFT in quenched gold imaged under this diffraction condition. Note that the contrast of even large SFT may be very weak. Figure 5 shows smaller SFT in ion-irradiated silver imaged using three different $\{2\bar{2}0\}$ reflections. In each case the contrast comes primarily from the stacking faults not containing **g**, although their visibility is somewhat variable.

In most of the images of Figs. 2 and 3 the contrast of the stair-rods is relatively weak but visible. These dislocation images are not at the position of their projection, but are shifted sideways as a consequence of the x and y terms in $\frac{\partial\phi}{\partial x}$ and $\frac{\partial\phi}{\partial y}$ in the Howie–Basinski equations. As shown in Fig. 6 the displacements are in the –**g** direction. There is no corresponding shift in stacking-fault fringes. High-quality images of large SFT are rare in the literature. However the images shown in Fig. 7 taken from Ref. [14] do show evidence of this effect. Images calculated using the column approximation do not show this effect.

The contrast was also found to be sensitive to the deviation parameter. Figure 8 shows image simulations for a 10 nm SFT (upper row) and a 5 nm SFT (lower row) in Ag demonstrating the effect of a small change in deviation

[2] Normalisation of simulated images is of course an issue. In Fig. 2 and elsewhere there is no change in normalisation from one simulation to another. Generally we regard the contrast as very low if the maximum image intensity relative to background, $y = I_{max}/I_{background}$ is less than 3. If $3 < y < 10$ we consider that visibility is low, but the defect is likely to be detected. For a discussion see ref [4].

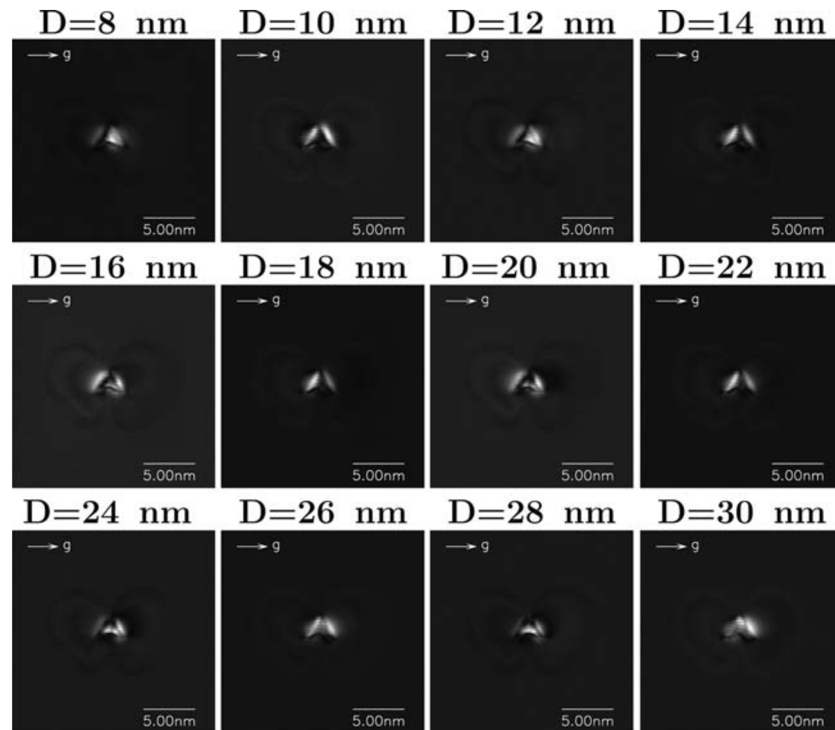

Fig. 3 The dependence of the contrast of a 3 nm SFT in copper on the defect depth *D*. Values of *D* are as shown above each simulated image. The foil is of thickness 57 nm, chosen to give good image contrast, and the SFT is imaged with **g** = $2\bar{2}0$ at **n** = [111]. The diffraction condition is (**g**, 3.25**g**), which is equivalent to $s_g = 0.2\ \text{nm}^{-1}$

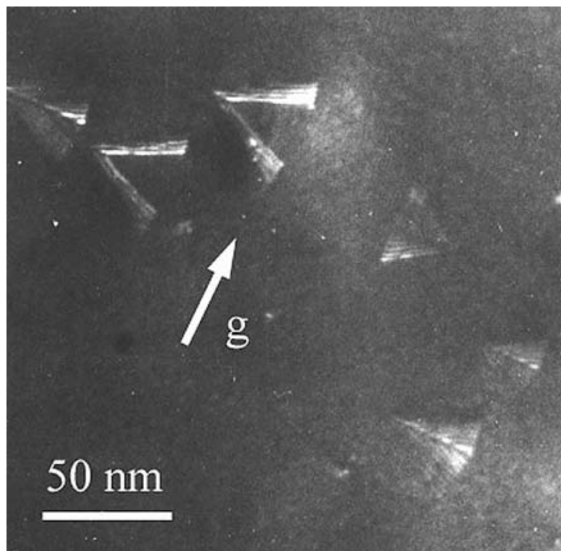

Fig. 4 Large SFT in quenched gold imaged using **g** = $2\bar{2}0$ under weak-beam conditions with $s_g = 2 \times 10^{-1}\ \text{nm}^{-1}$. Note the weak stacking fault contrast shown by several of the SFT. The two large SFT towards the top of the micrograph are truncated by the foil surface

parameter. The values of deviation parameter from left to right in each row are $s_g = 0.2$, 0.205 and 0.21 nm^{-1}. Corresponding experimental images are shown in Fig. 9. The strong dependence of the image contrast on s_g predicted by the simulations is borne out by the experiments. Images which are clearly identifiable as SFT under one condition (for example the upper circled defect in Fig. 9a) are far less clear in Fig. 9b, c. Most of the other defects in this field of view appear to be partially dissociated Frank loops rather than complete SFT. More systematic studies of the sensitivities of the contrast to the deviation parameter are shown for the alternative foil orientation below.

Foil normal **n** = [110] and diffraction vector **g** = 002

This diffraction geometry has often been used to investigate small clusters in irradiated fcc metals, see e.g. Ref. [5] and so was chosen to investigate systematically the weak-beam contrast of Frank loops [4]. This was also the geometry investigated by Satoh et al. [7] in the most extensive previous investigation of the weak-beam contrast of SFT. Simulations of weak-beam images of SFT under this condition are shown in Figs. 10–12. Figure 10 shows simulated images for SFT with different edge lengths l ranging from 10 nm to 2 nm. In each case images are shown for four values of the foil thickness. In this orientation two of the stacking-fault faces are edge-on, and two are shallowly inclined and overlapping, leading to rather more complex contrast features than in the orientation considered above. The images of larger SFT appear as fairly well defined triangles, with intensity, which may be above or below background. The images of SFT of size 3 nm or smaller SFT are less distinct and could be confused with the images of small Frank loops under these conditions, see [4]. The contrast of very small SFT is sometimes very weak, such that in practice they would

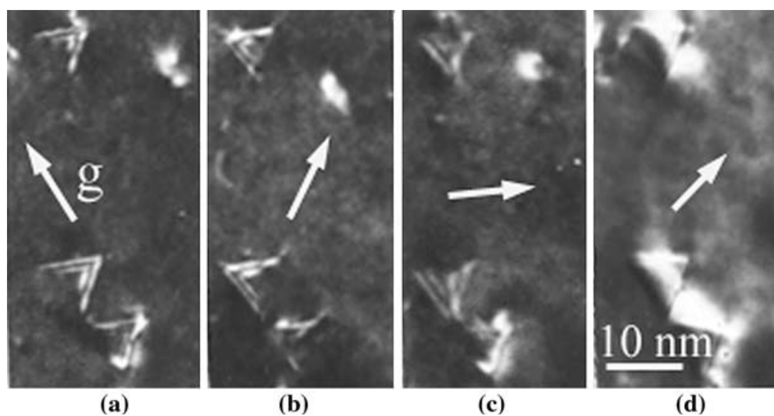

Fig. 5 SFT in ion-irradiated silver, imaged in (**a**) **g** = $2\bar{2}0$ (**b**) **g** = $0\bar{2}2$ (**c**) **g** = $\bar{2}02$ with the foil oriented close to [111], and (**d**) **g** = 002 with the foil oriented close to [110]. In the weak-beam images of (**a**)–(**c**) the SFT are imaged mainly by stacking-fault fringes on the two inclined faces of fault not containing **g**. In (**d**) the SFT are imaged under dark-field dynamical conditions, and they show characteristic black-white contrast

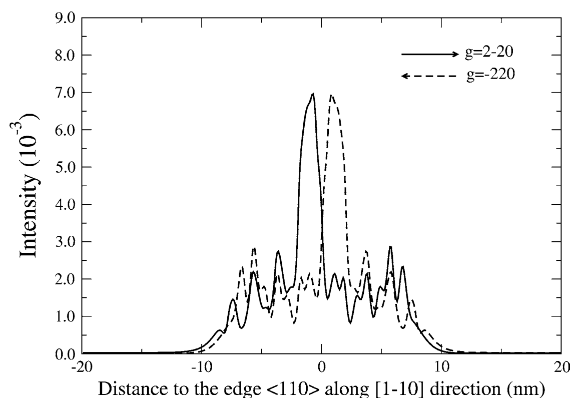

Fig. 6 Intensity profiles parallel to [$1\bar{1}0$] for Fig. 2 (**e**) and (**j**), showing the displacement of the images of the stair-rod dislocations in the direction –**g** when imaged using **g** = ± $2\bar{2}0$

likely not be visible. Figure 11 shows the dependence of the contrast on foil thickness and diffraction condition of an SFT of edge-length 5 nm situated at a depth of 30 nm. Again it can be seen that the contrast shape is generally triangular, with contrast either predominantly above or below background, and with very weak-contrast for some combinations of foil thickness and diffraction condition. The dependence of the contrast on defect depth D is shown in Fig. 12. The contrast changes significantly for changes in D as little as 1 nm. A comparison of experimental and simulated images for the (**g**, 5**g**) condition is shown in Fig. 13. The agreement is good. The circled regions in the experimental micrograph each contain two SFT, one of which appears as a light triangle and the other as a dark triangle. This can only be because they lie at different depths since the foil thickness must be the same for each pair. This is in accord with the inset simulations.

Discussion

Visibility of SFT and optimum imaging conditions

The simulations and experiments show that the visibility of SFT depends on the imaging conditions, particularly the combination of foil thickness and deviation parameter, and the SFT depth. Very small SFT may be effectively invisible if they happen to lie in a thickness fringe maximum or at a depth where stacking-fault contrast is weak. The dependence on the foil thickness is similar to that found for Frank loops [4]. The sensitivity to the depth is different from the result found for Frank loops, where the contrast is relatively insensitive to the loop depth [4]. It arises because stacking-fault fringes vary with depth and stacking-fault contrast is weaker nearer the foil centre than close to the foil surfaces because of anomalous absorption effects (see

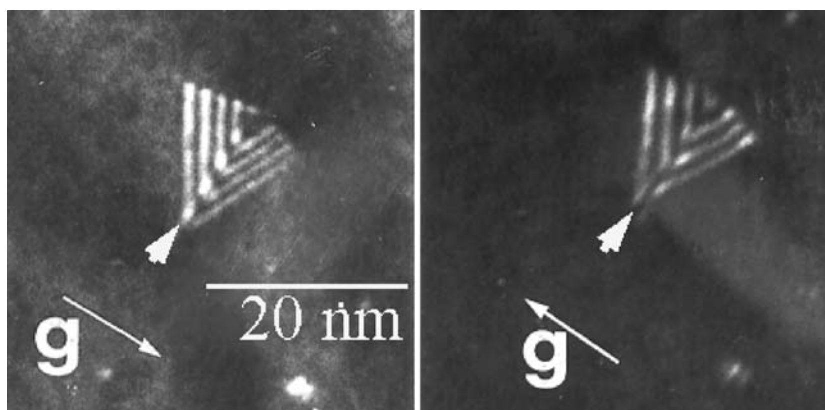

Fig. 7 Weak-beam images of SFT in quenched gold imaged with **g** = ± $2\bar{2}0$ and $s_g \approx 2 \times 10^{-1}$ nm^{-1}, taken from [14]. The contrast arising from the stair-rod dislocation is arrowed

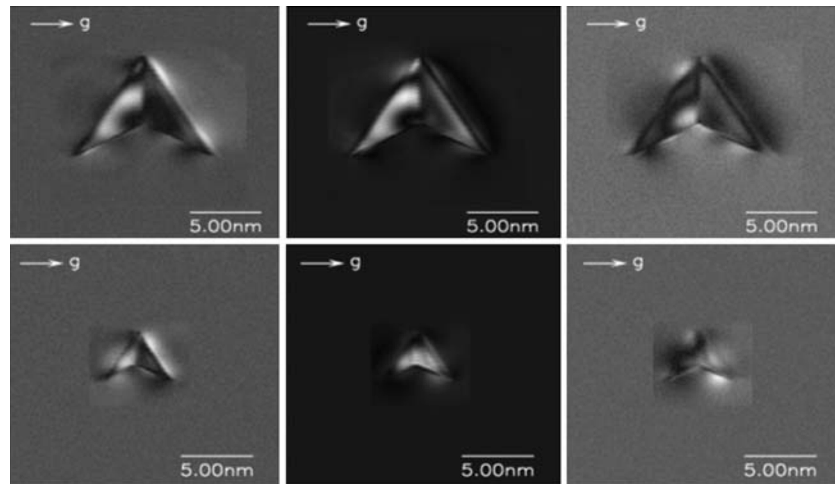

Fig. 8 Weak-beam image simulations of a 10 nm SFT (upper row) and a 5 nm SFT (lower row) in silver showing the effect of a small change in deviation parameter. The values of deviation parameter from left to right in each row are $s_g = 0.2$, 0.205 and 0.21 nm^{-1} according to the experimental conditions of Fig. 9. Foil thickness 60 nm defect depth 30 nm

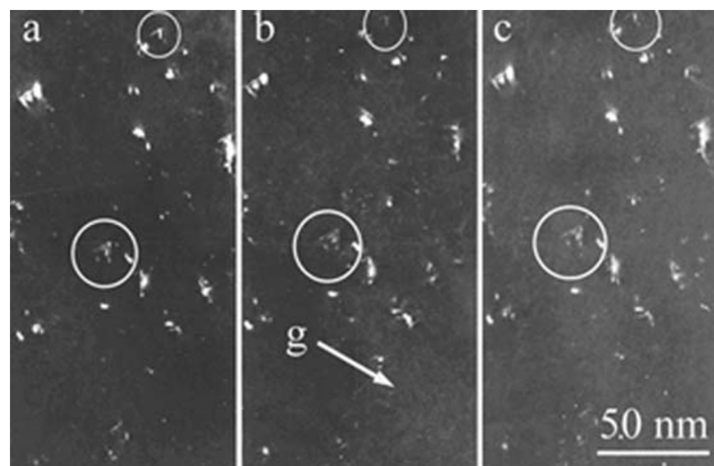

Fig. 9 Defects in ion-irradiated silver imaged in weak-beam with **g** = $2\bar{2}0$ at [111] with small changes in deviation parameter: (**a**) $s_g = 2.0 \times 10^{-1}$ nm^{-1}, (**b**) $s_g = 2.05 \times 10^{-1}$ nm^{-1}, (**c**) $s_g = 2.1 \times 10^{-1}$ nm^{-1}. The circled defects appear to be complete or nearly-complete SFT

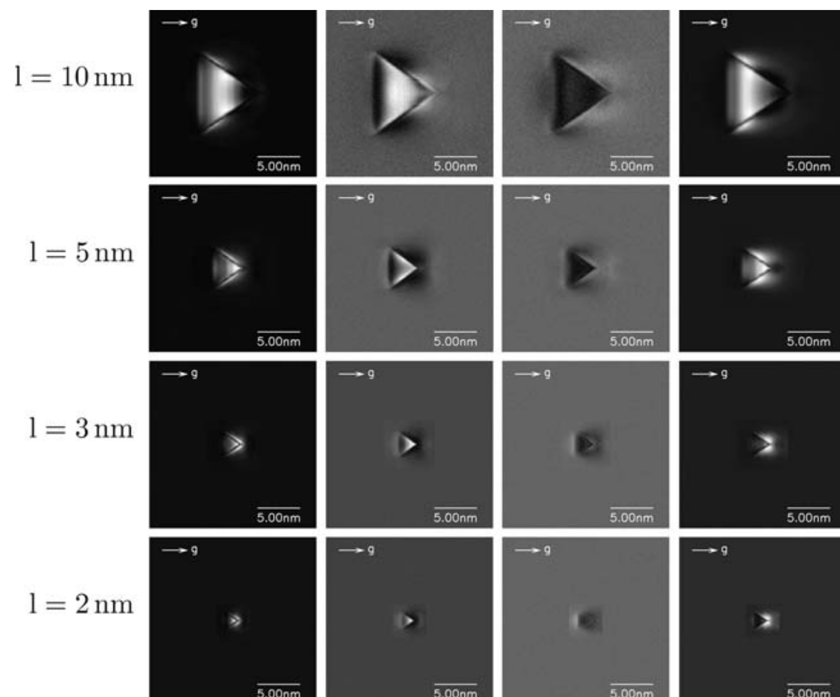

Fig. 10 Dependence of the contrast on the SFT size for **g** = 002 at **n** = [110]. Each row of simulated weak-beam images corresponds to four different values of the foil thickness (from left to right 55.2, 56.8, 58.4 and 60.0 nm). Defect depth 30 nm. Diffraction condition (**g**, 4.50**g**). Simulation for copper

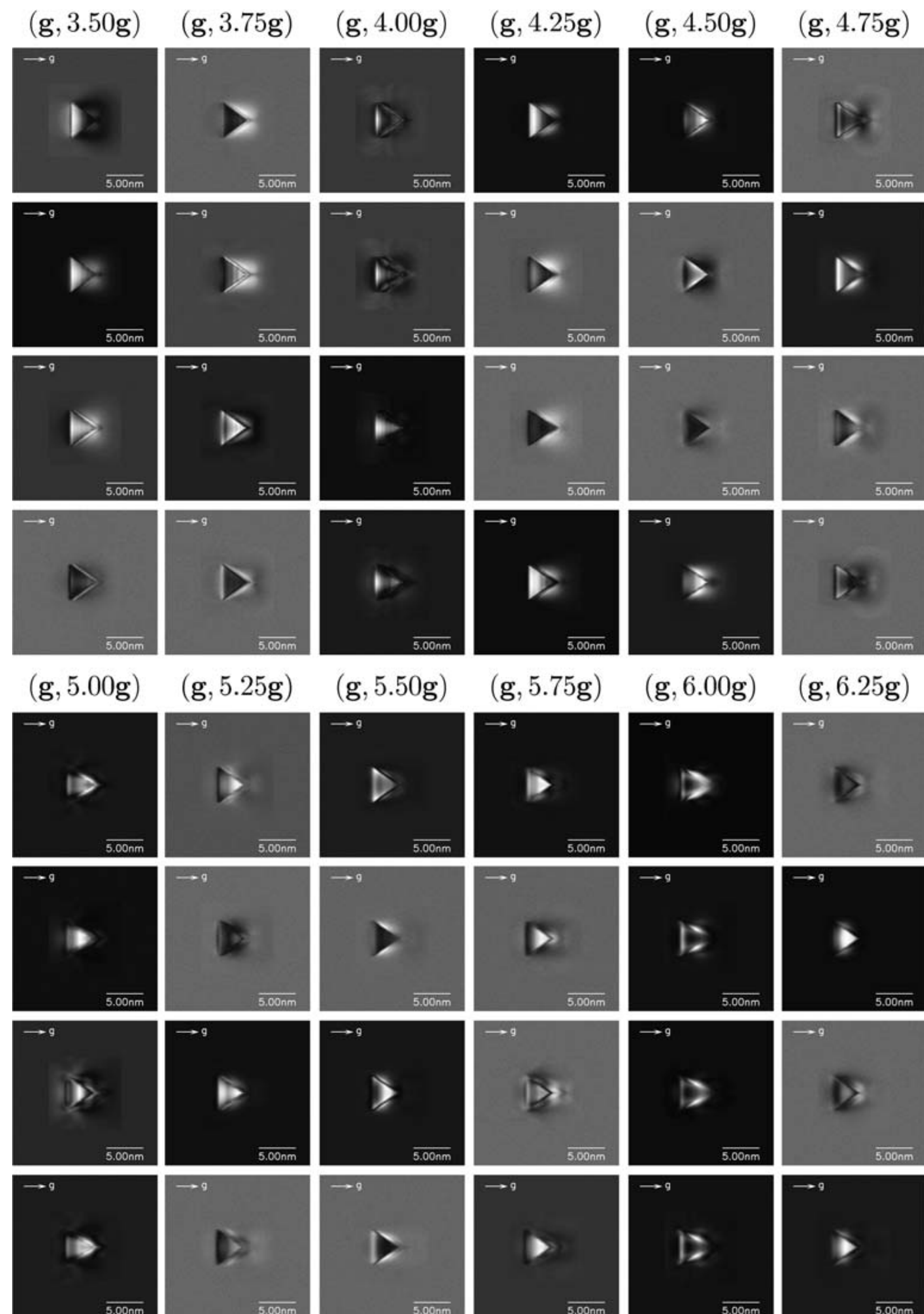

Fig. 11 Dependence of the contrast of a 5 nm SFT in copper on the diffraction condition and the foil thickness for **g** = 002 at **n** = [110]. The diffraction condition (**g**, n**g**) is shown at the top of each column of four images, which correspond to four different values of the foil thickness (from top to bottom of each column 55.2, 56.8, 58.4 and 60.0 nm). Defect depth 30 nm

e.g. [16]). As for small Frank loops [4], the detection of small SFT can be improved by taking several micrographs with different deviation parameters. These conclusions are in general agreement with those of Satoh et al. [7]. Both of the orientations we considered are suitable for imaging SFT, but the interpretation of images is perhaps more straightforward at a foil normal **n** = [111] and diffraction vector **g** = $\pm 2\bar{2}0$, because the stacking-faults in contrast do not overlap. Very small SFT imaged under both conditions may be difficult or impossible to distinguish from Frank loops, particularly if these are partially dissociated.

It is interesting to note that the image artefacts seen for Frank loops when imaged under (**g**, n**g**) diffraction conditions with integer n do not seem to occur for SFT. In the case of Frank loops extraneous contrast lobes occur, which are not associated with geometrical features of the loop [4]. For SFT the images for integral values of n are very similar to images for non-integral values (see for example Figs. 11

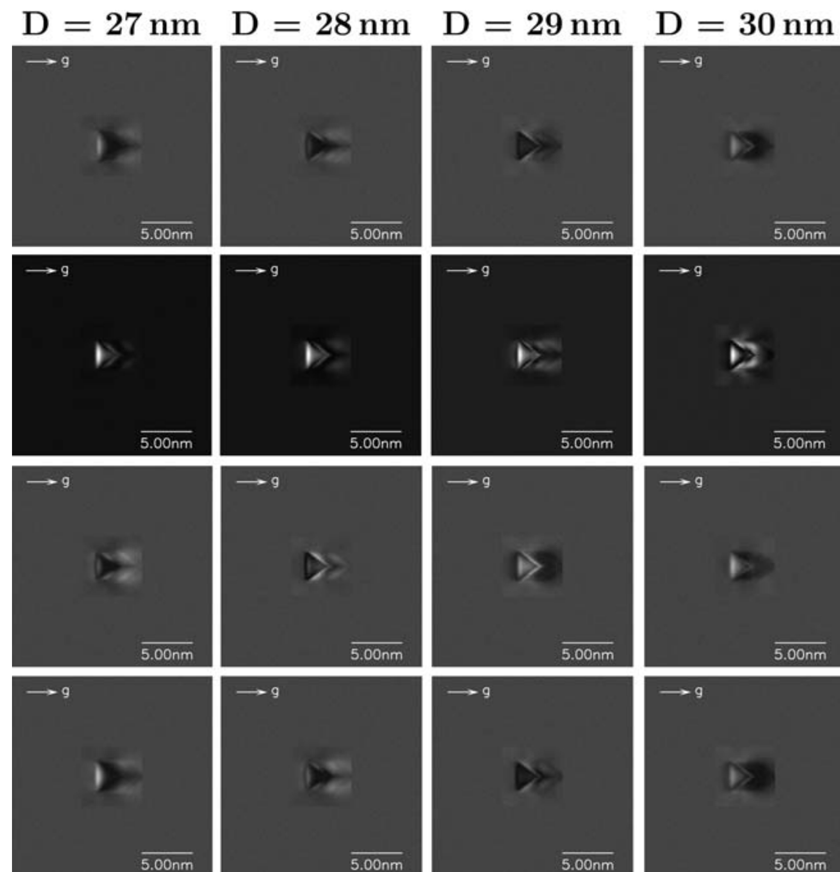

Fig. 12 Dependence of image contrast of a 3 nm SFT in copper on the defect depth *D*. Each column of four weak-beam images is for the value of *D* shown for four different foil thicknesses (from top to bottom, 55.2, 56.8, 58.4 and 60.0 nm). Diffraction vector **g** = 002 at **n** = [110]. Diffraction condition (**g**, 5.05 **g**)

and 13 for n = 5). The reason for this is unclear. In the case of loops it is preferable to avoid exciting higher-order reflections, and it was for this reason that most of our simulations were made for non-integral values of n.

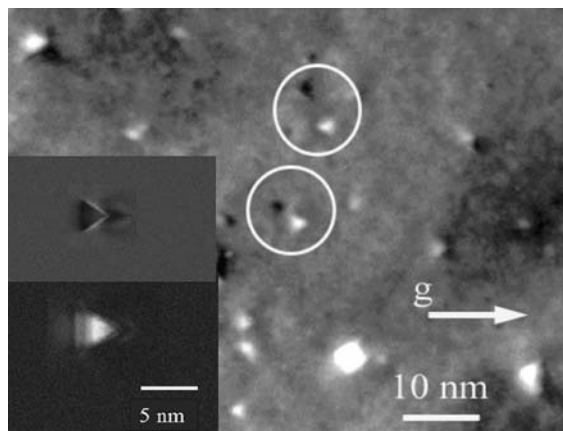

Fig. 13 Weak-beam micrograph of defects in copper irradiated with 750 MeV protons to a dose of 0.5 dpa at 90 °C [15]. The micrograph was taken in **g** = 002 with the foil oriented close to [110] with a (**g**, 5**g**) diffraction condition in a foil of thickness about 25 nm. The circles each contain images of two SFT, one visible as a white triangle and the other a dark triangle. Two simulated images for this condition, with different defect depths but the same foil thickness, are inset. Micrograph courtesy of Dr S J Zinkle

Sizing SFT

Weak-beam images of SFT obtained using **g** = $2\bar{2}0$ at **n** = [111] are dominated by stacking-fault fringes arising from the triangular inclined faces of fault, with the stair-rod dislocations making only a minor contribution to the total contrast. Small SFT, of edge-length $L \leq \xi_g^{\mathrm{eff}} \approx 5$ nm, generally show just one fringe from each inclined face. Larger SFT may show two or more fringes with depth periodicity ξ_g^{eff}. The images are generally smaller than the true SFT size, and are dependent on factors such as the deviation parameter and the defect depth and foil thickness. For different values of $|s_g|$, the fringes are displaced in depth, moving up or down the face of the fault Single weak-beam images may therefore give misleading impressions of the sizes of small SFT because the positions of the fringes on the fault faces can vary. This can be seen by comparing the experimental images of Fig. 7 which were taken with slightly different values of $|s_g|$. The simulations of Fig. 3 show the same effect for a small SFT. For images obtained in **g** = 002 at **n** = [110] the situation is similar, although in this case the contrast from the overlapping stacking-faults on the two shallowly-inclined {111} planes is broader. Again the image size is generally smaller than the true SFT size. This latter geometry was

investigated by Satoh et al. [7] using the multislice method to simulate the contrast of very small SFT and our findings are generally in good agreement with theirs.

For both orientations investigated, the image size is a reasonably good representation of the projected actual size for SFT larger than about 5 nm. The image size is typically smaller but within about 5% of the true SFT size for a 10 nm SFT and 10% for a 5 nm SFT. The error may be larger for smaller SFT.

Satoh et al. [7] have suggested that if micrographs of SFT are recorded for several different values of $|s_g|$, the largest image size might be expected to correlate reasonably well to the maximum extent of the fault. The *maximum* image size should therefore be taken to correspond to the true projected size of the SFT. Experimental studies of small (~2 nm) SFT in quenched silver imaged under a wide range of $|s_g|$, from two-beam ($|s_g| = 0$) to weak-beam with $|s_g| = 0.3\ nm^{-1}$, were in good accord with this hypothesis. The image sizes of *individual* SFT varied with deviation from the Bragg condition, but in each case showed a well-defined maximum. Overall, the visibility was best for $|s_g| \geq 0.2\ nm^{-1}$, but the a*verage* image sizes of about 300 SFT was only weakly dependent on $|s_g|$. Our simulations support this conclusion for both geometries investigated.

Summary and conclusions

1. Images of SFT have been simulated under weak-beam diffraction conditions for different foil orientations and imaging parameters. Generally the contrast is dominated by stacking-fault contrast, with relatively minor contributions from the stair-rod dislocations.
2. Good agreement between simulated and experimental images has been achieved in many cases.
3. The contrast is dependent on the foil thickness, defect depth and the diffraction conditions. For some combinations of these parameters the visibility may be low and small SFT may be effectively invisible.
4. Generally for SFT larger than about 5 nm the image size is a reasonably good representation of the projected actual size.
5. Small SFT can be better detected and their sizes estimated more accurately by taking several micrographs with different values of $|s_g|$. The maximum image size in the different micrographs is the best estimate of the true SFT size.
6. Image shifts of dislocation images are predicted by the Howie–Basinski equations and found in practice.

Acknowledgements ZZ is grateful to the EURATOM/UKAEA Fusion Association for the provision of a studentship. He is also grateful to St Hugh's College for the award of a Wei Lun Scholarship. Work at UKAEAwas funded by EPSRC and EURATOM.

References

1. Howie A, Basinski ZS (1968) Phil Mag 17:1039
2. Zhou Z, Dudarev SL, Jenkins ML, Sutton AP (1973) Proceedings of EMAG Oxford, Inst. Physics Conf. Ser.179, p 203
3. Zhou Z, Dudarev SL, Jenkins ML, Sutton AP, Kirk MA (2004) Mat Res Soc Symp Proc 792:491
4. Zhou Z, Jenkins ML, Dudarev SL, Sutton AP, Kirk MA (2006) Phil Mag, in press
5. Jenkins ML, Kirk MA, Fukushima H (1999) J Electron Microsc 48:323
6. Saldin DK, Stathopoulos AY, Whelan MJ (1979) Phil Trans R Soc A 292:523
7. Satoh Y, Taoka H, Kojima S, Yoshii T, Kiritani M (1994) Phil Mag A 70:869
8. Schäublin R, Almazouzi A, Dai Y (1993) Mat Sci Eng A 164:373
9. Schäublin R, Dai Y, Osetsky Y (1998) In Electron Microscopy, Proc. ICEM 14 (Cancun, Mexico) Symposium C, vol 1, p 173
10. Yoffe EH (1960) Phil Mag 5:161
11. Saldin DK, Whelan MJ (1979) Phil Trans R Soc A 292:513
12. Viguir B, Hemker KJ, Vanderschaeve G (1994) Phil Mag A 69:19
13. Jenkins ML (1974) Phil Mag 29:813
14. Jenkins ML, Kirk MA (2001) Characterisation of radiation damage by transmission electron microscopy. Institute of Physics Publishing, ISBN 0 7503 0748 X, p 121
15. Zinkle SJ, Matsukawa Y (2004) J Nucl Maert 88:329
16. Hirsch PB, Howie A, Nicholson RB, Pashley DW, Whelan MJ (1977) Electron microscopy of thin crystals, revised edition, Robert. E. Krieger Publishing Company, chapter 10